Dalton Transactions

Quaternary Cerium(IV) Containing Fluorides Exhibiting Ce3F16 Sheets and Ce6F30 Frameworks

Journal:	*Dalton Transactions*
Manuscript ID	DT-ART-02-2020-000616.R1
Article Type:	Paper
Date Submitted by the Author:	06-Apr-2020
Complete List of Authors:	Ayer, Gyanendra; University of South Carolina, Department of Chemistry and Biochemistry Klepov, Vladislav; University of South Carolina, Department of Chemistry and Biochemistry Pace, Kristen; University of South Carolina, Zur Loye, Hans-Conrad; University of South Carolina, Department of Chemistry and Biochemistry

Quaternary Cerium(IV) Containing Fluorides Exhibiting Ce_3F_{16} Sheets and Ce_6F_{30} Frameworks

Gyanendra B. Ayer, Vladislav V. Klepov, Kristen A. Pace, and Hans-Conrad zur Loye*

Department of Chemistry and Biochemistry, University of South Carolina, 631 Sumter Street, Columbia, SC, United States
*e-mail: zurloye@mailbox.sc.edu

Abstract

A series of new Ce(IV) based fluorides with two different compositions, $Cs_2MCe_3F_{16}$ (M = Ni^{2+}, Co^{2+}, Mn^{2+}, and Zn^{2+}) and $Na_3MCe_6F_{30}$ (M = Al^{3+}, Ga^{3+}, Fe^{3+}, and Cr^{3+}) were synthesized as high quality single crystals via a mild hydrothermal route. The compounds with the composition $Cs_2MCe_3F_{16}$ (M = Ni^{2+}, Co^{2+}, Mn^{2+}, and Zn^{2+}) crystallize in the hexagonal crystal system with space group $P6_3/mmc$ and are isotypic with the uranium analogs, whereas the $Na_3MCe_6F_{30}$ (M = Al^{3+}, Ga^{3+}, Fe^{3+}, and Cr^{3+}) compounds crystallize in the trigonal space group $P\bar{3}c1$ and are isotypic with the uranium and thorium analogs $Na_xMM'_6F_{30}$ (M' = Th, U). The $Cs_2MCe_3F_{16}$ compounds exhibit a complex 3D crystal structure constructed of edge-sharing cerium trimers, in which all three Ce atoms share a common μ_3-F unit. The $Na_3MCe_6F_{30}$ compounds are constructed of edge- and vertex-sharing cerium polyhedra connected to each other to form $Ce_6F_{30}^{6-}$ framework, which can accommodate only relatively smaller trivalent cations (M^{3+} = Al^{3+}, Ga^{3+}, Fe^{3+}, and Cr^{3+}) as compared to uranium and thorium analogs. Magnetic susceptibility measurements were carried out on the samples of $Cs_2MCe_3F_{16}$ (M = Ni^{2+} and Co^{2+}), which exhibit paramagnetic behavior.

Introduction

The importance of optical materials in the modern technological applications, particularly in LED devices and upconversion materials, resulted in the development of a number of new classes of compounds for optical applications.[1–4] Oxides have attracted a lot of the attention due to their stability and the relative ease of doping them with lanthanide cations, such as Ce^{3+}, Eu^{3+}, and Tb^{3+}.[5–13] Another direction in developing new matrices for optical materials are fluorides and mixed halides, which offer a good platform for the design of new rigid and stable frameworks.[14–17] Several fluoride matrices have been extensively studied for potential bioimaging and LED applications, in particular, lanthanide-doped CaF_2,[18] $KMnF_3$,[19,20] YF_3,[21] $BaYF_5$,[22] and $LiYF_4$[23], which are promising due to their sharp f–f emission peaks, a long photoluminescence (PL) lifetime, low toxicity, and high resistance to photo-bleaching. For the efficient upconversion luminescence, the rare earth fluorides, such as $NaYF_4$ and $NaGdF_4$, that belong to AREF$_4$ (A = alkali metal, RE = rare earth) fluoride family have been used as host matrices for the Ln^{3+} doping because of their high chemical stability and intrinsic low phonon energies (<350 cm^{-1}).[24–30] For example, $KGdF_4$:Ln^{3+} nanocrystals can be used in bioprobes containing Gd^{3+} as a sensitizer,[31] while lanthanide-doped KGd_2F_7 nanocrystals, which were synthesized by a facile decomposition method, display characteristic downshifting and upconverting luminescence ranging from the visible to near-infrared spectral regions and can be employed for diverse applications, such as sensing, optogenetics and nano-photonics.[32] The use of fluorides is not limited to the rare earth elements as some other elements, such as Sc and Bi, can be employed to create host materials for Ln^{3+} doping to achieve an intense luminescence. For example, a novel hexagonal nanocrystals of $NaBiF_4$:Yb^{3+}/Er^{3+} and KSc_2F_7:Yb^{3+}/Er^{3+} show excellent upconversion luminescence.[33,34] Furthermore, the red emitting Mn^{4+} doped fluorides such as K_2SiF_6, K_2TiF_6, Rb_2GeF_6, Cs_2GeF_6, Cs_2HfF_6, $BaSnF_6$, $BaTiF_6$ are an important class of materials for LED lighting and displays.[35] All these examples demonstrate the importance of developing new fluoride host matrices for the further development of optical materials.

The design of new fluorides requires the development of new synthetic procedures that would enable the efficient formation of the target phases. The mild hydrothermal route has been shown as an extremely productive and convenient strategy for the synthesis of new fluorides, resulting in the formation of high quality single crystals that can be readily used for single crystal

X-ray analysis.[36-39] It also eliminates the use of highly toxic and corrosive HF and F_2 gases. A good example of how this approach can be employed for the synthesis of an extended family of compounds is the $Na_xMM'_6F_{30}$ (M is a di- or trivalent metal cation, M' is a tetravalent cation) structure type that can host 17 and 11 elements in the thorium and uranium(IV) frameworks, respectively.[40-42] Although these compounds were found to be very stable and form readily under various synthetic conditions, their cerium analogs have never been reported. Moreover, their exceptional stability (these compounds do not dissolve even in nitric acid)[43] demonstrate their potential for their use as functional materials. Recently, we have shown that the size of the tetravalent cation in the $Na_nMAn_6F_{30}$ families dictates the maximum size of the cation that can occupy the M site. The framework expansion using the larger Th^{4+} cation allowed for incorporation of even some Ln atoms (Tm and Lu), while the M cation size tolerance in the $Na_nMU_6F_{30}$ series falls somewhere in between Sc and the rare earth elements. This observation motivated us to pursue the synthesis of the Ce(IV) analogs of these compounds along with those belonging to a second structural fluoride family, $Cs_2MCe_3F_{16}$, to follow this trend and probe the size influence on the stability of $Na_3MCe_6F_{30}$ compounds.

In this report, we describe the synthesis and characterization of 8 new cerium fluoride compounds that belong to two structure types, $Na_3MCe_6F_{30}$ (M = Al^{3+}, Ga^{3+}, Fe^{3+}, and Cr^{3+}) and $Cs_2MCe_3F_{16}$ (M = Ni^{2+}, Co^{2+}, Mn^{2+}, and Zn^{2+}). As the Ce^{4+} cation is smaller than the U^{4+} and Th^{4+} cations (their Shannon ionic radii are 1.02, 1.05 and 1.09 Å, respectively)[44] the use of cerium should result in a smaller $Na_nMCe_6F_{30}$ framework that can accommodate only small M cations. This hypothesis is supported by our synthetic results that led to our characterization of the new compounds by single crystal and powder X-ray diffraction, UV-vis spectroscopy, and magnetic susceptibility measurements.

Experimental section

Reagents

NaF(Alfa Aesar, 99%), CsF (Alfa Aesar, 99.9%), CeO_2 (Alfa Aesar, 99.9%), NiF_2 (Alfa Aesar, 99%), CoF_2 (Alfa Aesar, 98%), MnF_2 (Alfa Aesar, 99%), ZnF_2 (Alfa Aesar, 99%), Al_2O_3 (Johnson Matthey, 99.9%), Ga_2O_3 (Alfa Aesar, 99.9%), FeF_3 (Strem, 99%), $CrF_3 \cdot xH_2O$ (Alfa Aesar), and HF (EMD, 49%) were used as received.

Warning! HF should only be handled in a well-ventilated space and proper safety precautions must be used as it is highly corrosive and toxic. If contact with the liquid or vapor occurs, proper treatment procedures should immediately be followed.

Synthesis

The title compounds were grown as single crystals by utilizing a mild hydrothermal synthetic approach. For the preparation of $Cs_2MCe_3F_{16}$ (M= Ni, Co, Mn, and Zn), 2 mmol of CeO_2, 2 mmol of CsF, and 2 ml of 49% HF were combined with 1 mmol of NiF_2, CoF_2, MnF_2, or ZnF_2 respectively. For the preparation of $Na_3MCe_6F_{30}$ (M = Al, Ga, Fe, and Cr), 2 mmol of CeO_2, 2 mmol of NaF, and 2 ml of 49% HF were combined with 1 mmol of Al_2O_3, Ga_2O_3, FeF_3, and $CrF_3 \cdot xH_2O$ respectively. The respective solutions were placed into 23 ml PTFE-lined autoclaves. The autoclaves were sealed, heated to 200°C at a rate of 5 °C min^{-1}, held at this temperature for one day, and cooled to room temperature at a rate of 6 °C h^{-1}. The mother liquor was decanted from the product, which was isolated by filtration and washed with distilled water and acetone. In all cases for $Cs_2MCe_3F_{16}$ (M= Ni, Co, Mn, and Zn), the reaction yielded hexagonal plate-shaped crystals that consist of light-green crystals for Ni, pink crystals for Co, reddish-brown crystals for Mn and colorless crystals for Zn in an approximately 10% yield based on cerium. For $Na_3MCe_6F_{30}$ (M = Al, Ga, Fe, and Cr), the reactions yielded colorless block crystals for M = Al, Ga, and Fe and light-green translucent rod-shaped crystals for Cr in an approximately 60% yield based on CeO_2.

Single Crystal X-ray Diffraction

X-ray intensity data sets were collected on all single crystals at 300(2) K on a Bruker D8 QUEST diffractometer equipped with an Incoatec IμS 3.0 microfocus radiation source (Mo Kα, λ = 0.71073 Å) and a PHOTON II area detector. The raw area detector data frames were reduced and corrected for absorption effects with the SAINT and SADABS programs.[45,46] Final unit cell parameters were determined by least-squares refinement of a large number of reflections taken from the data set. Direct methods structure solution, difference Fourier calculations, and full- matrix least-squares refinement against F^2 were performed with SHELXL software. [47]

Powder X-ray Diffraction

Powder X-ray diffraction (PXRD) data, covering the angular range of 5 to 65° in 2θ with a step size of 0.04°, were collected for phase purity confirmation on a Bruker D2 PHASER diffractometer utilizing Cu Kα radiation. No impurities were observed in the diffraction patterns, (Figure S1 and S2).

Optical Properties

UV−vis spectra were recorded using a PerkinElmer Lambda 35 UV/visible scanning spectrophotometer used in the diffuse reflectance mode equipped with an integrating sphere. Diffuse reflectance spectra were recorded in the 200−900 nm range. Reflectance data were converted to absorbance by the instrument via the Kubelka−Munk function.[48] All optical measurements were performed on polycrystalline powders obtained by grinding the product single crystals, (Figure S3).

Magnetism

The magnetic properties of the ground samples were measured using a Quantum Design MPMS 3 SQUID magnetometer. Temperature-dependent field-cooled (FC) and zero-field-cooled (ZFC) susceptibility measurements were performed from 2 to 300 or 375 K in an applied field of 0.1 T. The raw data were corrected for radial offset and sample shape effects according to the method described in the literature. [49]

Table 1. Crystallographic data for $Cs_2MCe_3F_{16}$ (M= Ni, Co, Mn, and Zn), $Na_3MCe_6F_{30}$ (M = Al, Ga, Fe, and Cr)

	$Cs_2NiCe_3F_{16}$	**$Cs_2CoCe_3F_{16}$**	**$Cs_2MnCe_3F_{16}$**	**$Cs_2ZnCe_3F_{16}$**	**$Na_3AlCe_6F_{30}$**	**$Na_3GaCe_6F_{30}$**	**$Na_3FeCe_6F_{30}$**	**$Na_3CrCe_6F_{30}$**
Formula weight	1048.89	1049.11	1045.12	1055.55	1506.67	1549.41	1535.54	1531.69
Crystal system	Hexagonal				Trigonal			
Space group, Z	$P6_3/mmc$				$P\bar{3}c1$			
a, Å	7.8687 (2)	7.8823 (2)	7.9014 (2)	7.8769 (2)	9.6715 (2)	9.7126 (3)	9.7288 (2)	9.7142 (3)
b, Å	7.8687 (2)	7.8823 (3)	7.9014 (2)	7.8769 (2)	9.6715 (2)	9.7126 (3)	9.7288 (2)	9.7142 (3)
c, Å	12.8302 (3)	12.9303 (3)	13.0931 (4)	12.9013 (3)	12.7479 (3)	12.7972 (4)	12.8247 (3)	12.7980 (5)
γ, deg	120	120	120	120	120	120	120	120
V, Å^3	687.97 (4)	695.74 (4)	707.91 (4)	693.23 (4)	1032.66 (5)	1045.48 (7)	1051.23 (5)	1045.89 (8)
ρ_{calcd}, g/cm^3	5.063	5.008	4.903	5.057	4.846	4.922	4.851	4.864
Radiation (λ, Å)	MoKα(0.71073)							
μ, mm^{-1}	16.470	16.125	15.568	16.717	13.310	14.365	13.695	13.591
T, K	300(2)							
Crystal dim.,mm^3	0.03×0.03×0.01	0.03×0.03×0.01	0.03×0.02×0.02	0.02×0.01×0.01	0.07×0.07×0.06	0.08×0.06×0.01	0.07×0.07×0.06	0.08×0.06×0.01
2θ range, deg.	2.99 – 33.08	2.98 – 33.10	2.98 – 33.09	2.99 – 33.13	2.43 – 36.32	2.42 – 36.37	2.42 – 36.29	2.42 – 36.33
Reflections collected	10772	18480	10749	16989	20879	22864	22387	20004
Data/restraints/ parameters	335/28/0	338/28/0	347/28/0	480/29/0	1249/63/0	1030/63/0	1032/0/63	1029/0/62
R_{int}	0.0305	0.0280	0.0354	0.0358	0.0284	0.0401	0.0271	0.0409
Goodness of fit	1.148	1.220	1.090	1.155	1.082	1.058	1.156	1.187
$R_1(I > 2\sigma(I))$	0.0231	0.0113	0.0130	0.0113	0.0097	0.0112	0.0090	0.0141
wR_2 (all data)	0.0450	0.0236	0.0299	0.0237	0.0281	0.0246	0.0206	0.0299

Results and Discussion

Crystal Growth

To determine the range of Ce(IV) fluoride formation as a function of cation size, a mild hydrothermal synthetic route was used at a temperature of 200 °C to synthesize a series of novel Ce(IV) containing fluorides, $Cs_2MCe_3F_{16}$ (M= Ni, Co, Mn, and Zn) and $Na_3MCe_6F_{30}$ (M = Al, Ga, Fe, and Cr). The existence of these cerium fluoride phases was anticipated given the reported uranium and thorium series, $Cs_2MU_3F_{16}$ (M = Mn, Co, Ni, and Zn) and $Na_nMM'_6F_{30}$ (n = 3 or 4, M is a tri- or divalent 3d metal, and M' = U, Th), and the fact that the ionic radii of Ce(IV), U(IV) and Th(IV) are very similar.[40-42,50] For the preparation of $Cs_2MCe_3F_{16}$ (M= Ni, Co, Mn, and Zn), the molar ratios of the cerium, cesium, and the divalent metal precursors were optimized to obtain phase pure samples in every case, except for the Mn containing analog. Any attempt to optimize the reaction conditions for obtaining a phase pure sample of the Mn analog was not successful, and the product always contained a minor fraction of a CeF_3 impurity. For the synthesis of $Na_3MCe_6F_{30}$ (M = Al, Ga, Fe, and Cr) series, we utilized the reaction conditions similar to those reported for the synthesis of the thorium analogs, $Na_3MTh_6F_{30}$ (M = Al, Ga, Fe, and Cr).[40]

The use of hydrofluoric acid in the reaction mixture maintains a favorable pH environment ($\sim 1-2$)[30] that facilitates digestion of the CeO_2 precursor and that leads to the formation of a stable cerium/transition metal fluoride framework. Interestingly, our initial attempts to prepare $Cs_2MCe_3F_{16}$ (M= Ni, Co, Mn, and Zn) using divalent metal acetate precursors resulted in the formation of CeF_3 as the major product, while the use of divalent metal fluoride precursors resulted in phase pure samples of the target compounds. This effect is reminiscent of one observed in uranium chemistry, where an excess of fluoride anions in the presence of the relatively weak acetate reducing agent leads to the reduction of U(VI) and the stabilization of the +4 oxidation state for uranium. In an analogous process, Ce(IV) reduces in the presence of acetate anions, transforming CeO_2 to CeF_3. Given that no other Ce(III) fluoride phase was observed in the present studies, one can surmise that CeO_2 reduction is favored by the thermodynamic stability of CeF_3 phase rather than a high redox potential of CeO_2 under the reaction conditions, although one cannot draw a definitive conclusion based on our experiments. However, it is noteworthy that Kolis et al. observed a similar effect in a reaction of CeF_4 with various alkali cation mineralizers, such as TlF,

KF, and NH_4F, at 250 °C, where no apparent reducing agent was present, indicating an increasing oxidizing power of Ce^{4+} in fluoride media with increasing temperature.[37]

For the $Na_3MCe_6F_{30}$ (M = Al, Ga, Fe, and Cr) series, regardless of our numerous attempts to incorporate Ti^{3+} and larger trivalent cations into the Ce_6F_{30} framework, no additional analogs were obtained. Moreover, the reactions in the presence of divalent metal fluorides, such as NiF_2 and CoF_2, did not result in any $Na_4MCe_6F_{30}$ phase, which is surprising given the exceptional stability of the thorium and uranium analogs.[40,42] Instead, the ternary $Na_7Ce_6F_{31}$ composition forms along with a minor fraction of CeF_3, highlighting the stability of the former phase over $Na_4MCe_6F_{30}$ under the reaction conditions used. One possible source of its stability (versus U and Th analogs) are the similar sizes of the Na^+ and Ce^{4+} cations that result in substitutional disorder across all three unique metal sites in the structure of $Na_7Ce_6F_{31}$.[37] It appears that the largest trivalent cation that can be incorporated into the structure is iron, a significant decrease in the range of $Na_xMM'_6F_{30}$ formation as a function of trivalent cation size from ~0.80 to ~0.645 Å (the Shannon radii of In^{3+} and Fe^{3+} cation with CN = 6)[44] for M' = U and Ce respectively. This is in good agreement with the previously observed trend that the larger Th^{4+} cation forms a framework with larger pores that can accommodate larger M cations versus the analogous U framework. [40,41] As the Ce^{4+} size is even smaller (~1.02 versus 1.05 Å for Ce(IV) and U(IV), respectively), it can only accommodate cations as large as Fe^{3+} on the M site (Figure 1).

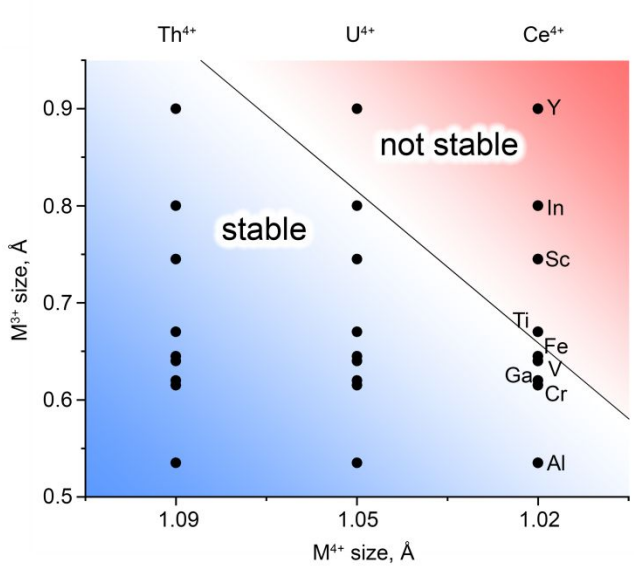

Figure 1. The size of trivalent cations M^{3+} (M = Al, Cr, Ga, V, Fe, Ti, Sc, In, and Y) plotted against the size of the tetravalent framework forming cations Th^{4+}, U^{4+}, and Ce^{4+}. The line indicates the position of a phase boundary for each series at the given reaction conditions.

Structure Description

$Cs_2MCe_3F_{16}$ (M= Ni, Co, Mn, and Zn): The compounds crystallize in the hexagonal crystal system with the space group *P*6$_3$/*mmc* and are isotypic with the uranium analogs, $Cs_2MU_3F_{16}$ (M= Ni, Co, Mn, Mg, and Zn).[50] The asymmetric unit consists of one cerium, one divalent metal, one cesium, and four fluorine atoms. The crystal structure is constructed of edge-sharing cerium trimers, in which all three Ce atoms share a common μ_3-F unit. Each trimer shares six edges with neighboring trimers to form a sheet that is perpendicular to the *c* axis. The divalent cations are located on top and below of each trimer, connecting successive sheets into a 3D framework with pores that are occupied by Cs atoms. The unit cell volume changes accordingly to the size of the divalent metal cations, decreasing from 707.91(4) Å^3 for M = Mn^{2+} (r(Mn^{2+}) = 0.83 Å[44] to 687.97(4) Å^3 (r(Ni^{2+}) = 0.69 Å). [44]

The cerium atoms form CeF_9 coordination polyhedra in the shape of a monocapped tetragonal antiprism with Ce–F bond distances ranging from 2.181(2) to 2.366(2) Å. Three cerium polyhedra connect through a common μ_3-F anion and share an edge with each other to form a Ce_3F_{22} cerium

trimer (Figure 2a), which edge shares to form a sheet perpendicular to the *c* axis. The divalent metal cations M^{2+} = Ni^{2+}, Co^{2+}, Mn^{2+}, and Zn^{2+} form almost regular octahedra with D_{3d} site symmetry (Figure 2b) and M–F bond lengths of 1.987(4), 2.017(2), 2.068(2), and 2.008(2) Å, respectively, and the F–M–F angles fall within the narrow range of 89.32(17)–90.60(6)°. The divalent metal cations connect the neighboring cerium trimers by corner-sharing through three fluoride ions of each trimer to form a column of successive trimers and M octahedra down the *c* axis (Figure 2c), linking the $[Ce_3F_{16}]^{4-}$ sheets into a framework (Figure 2d).

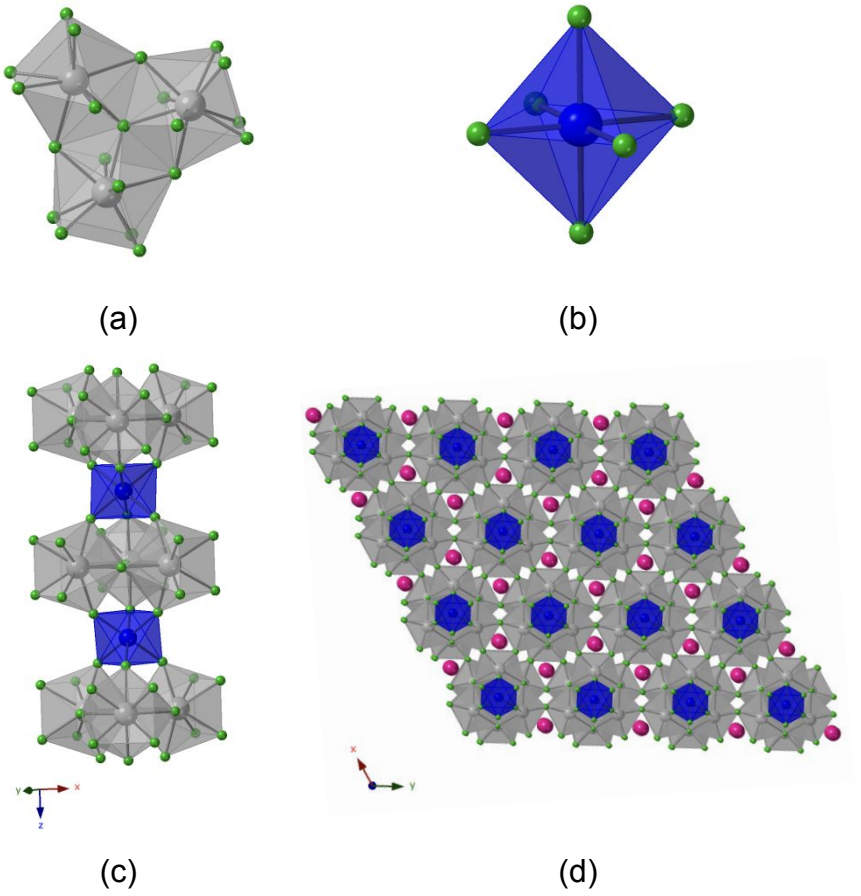

Figure 2. (a) A view of a MF_6 octahedron (M = Ni, Co, Mn, and Zn), (b) cerium trimer consisting of edge-sharing CeF_9 polyhedra, (c) sheet consisting of cerium trimers connected to each other by M^{2+} cations along the *c* axis, (d) a view of $Cs_2MCe_3F_{16}$ (M= Ni, Co, Mn, and Zn) structure along the *c* axis. The cerium, M (M = Ni, Co, Mn and Zn), cesium and fluorine atoms are shown in grey, deep blue, pink, and green, respectively.

$Na_3MCe_6F_{30}$ (M = Al, Ga, Fe, and Cr): All compounds crystallize in the trigonal space group $P\bar{3}$

*c*1 and are isotypic with the uranium and thorium analogs.[40,41] The asymmetric unit consists of one cerium, one trivalent metal ion, two sodium, and five fluorine atoms. The crystal structure is constructed of corner- and edge-sharing CeF_9 and MF_6 polyhedra to form a complex 3D framework structure, which contains the channels that are occupied by the sodium cations.

The cerium atoms form CeF_9 polyhedra (Figure 3a) in the shape of a distorted tricapped trigonal prism with Ce–F bond lengths ranging from 2.217(2) to 2.416(1) Å. By edge- and vertex-sharing, the cerium polyhedra connect to each other to form the $Ce_6F_{30}^{6-}$ framework containing two types of hexagonal channels. The Na(1) atoms occupy one type of channel, while the Na(2) atoms successively occupy the other one together with the trivalent atoms (Figure 3b). The trivalent cations form MF_6 octahedra with D_3 site symmetry. The M–F bond distances are 1.808(1), 1.879(1), 1.912(1), and 1.892(2) Å for Al, Ga, Fe, and Cr respectively.

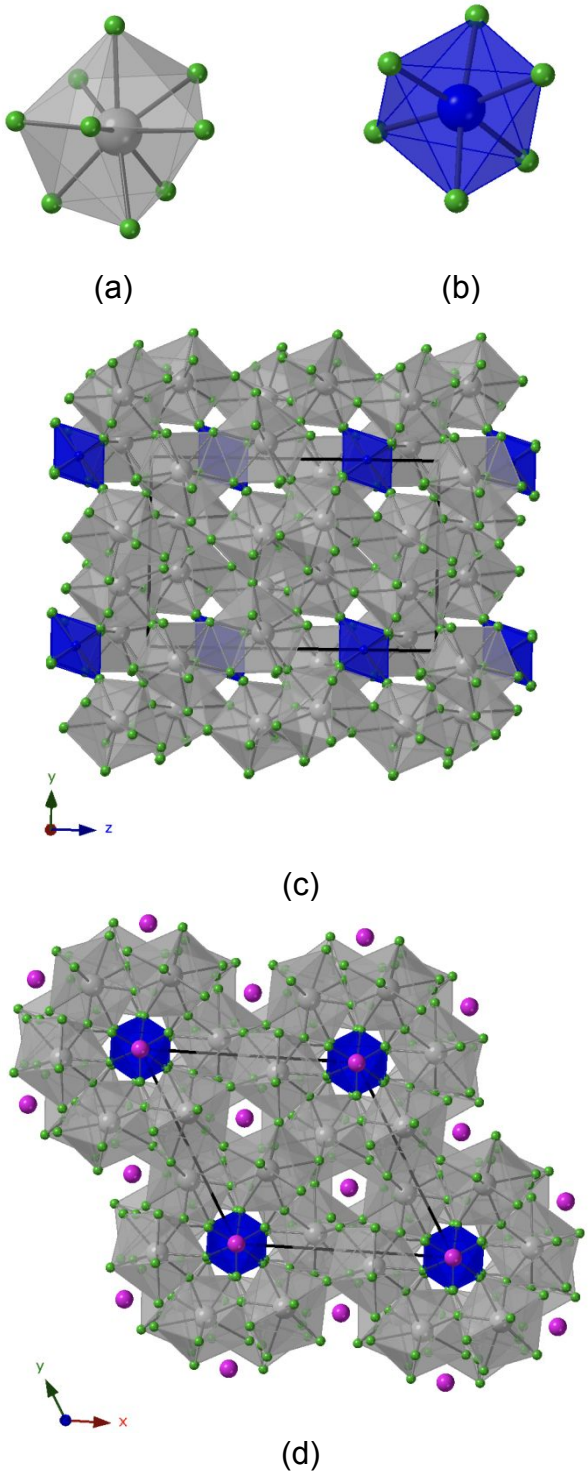

Figure 3. (a) A CeF_9 distorted tricapped trigonal prism, (b) metal ions (M = Al, Ga, Fe, and Cr) octahedron, (c, d) a view of $Na_3MCe_6F_{30}$ (M = Al, Ga, Fe, and Cr) structure along the *a* and *c* axes, respectively. The cerium, M (M = Al, Ga, Fe, and Cr), sodium and fluorine atoms are shown in grey, deep blue, pink, and green, respectively.

UV-Vis Diffuse Reflectance Spectroscopy

The optical measurements were performed on polycrystalline powders obtained by grinding the product single crystals of the compounds containing divalent cations, $Cs_2MCe_3F_{16}$ (M= Ni^{2+} and Co^{2+}). The various absorption bands are attributed to the d-d electronic transitions in the divalent metal ions, which were interpreted by the Tanabe-Sugano diagram.[51] In the nickel analog, the bands involve transitions to several excited states $^3T_{2g}$ (F), $^3T_{1g}$ (F) and $^3T_{1g}$ (P) from the ground state of $^3A_{2g}$ with a broad intense absorption band at 310 nm. The cobalt analog exhibits absorption bands in the 200–900 nm region due to transitions from the $^4T_{1g}$ ground state to $^4A_{2g}$ (F) and $^4T_{1g}$ (P) excited states with an intense peak at 338 nm (Figure S3), which is consistent with the reported spectra for divalent metal ions (M= Ni^{2+} and Co^{2+}).[51]

Magnetic Properties

The magnetic susceptibility data for $Cs_2MCe_3F_{16}$ (M= Ni^{2+} and Co^{2+}) were collected over the temperature range of 2 to 300 and 2 to 375 K (Figure 4). The $Cs_2NiCe_3F_{16}$ analog follows the Curie-Weiss law over a wide temperature range, while $Cs_2CoCe_3F_{16}$ deviates from Curie-Weiss behavior at temperatures below 50 K. The inverse susceptibility data were fitted to the Curie-Weiss law at temperatures above 50 and 100 K for M = Ni and Co, respectively, to derive the effective magnetic moments and the Weiss constants, which are given in Table 2 along with the calculated expected values for free ions.

The effective magnetic moment for $Cs_2NiCe_3F_{16}$ is virtually identical to the calculated spin only moment, 2.85 vs. 2.83 μ_B, with a slightly negative Weiss constant of -4.50 K, which is indicative of weak antiferromagnetic interactions between the nickel cations, although there are no apparent magnetic transitions down to 2 K. The derived magnetic moment of 5.34 μ_B found for the Co analog is significantly larger than a calculated spin only value of 3.87 μ_B, which is indicative of spin-orbit coupling that is typical for the Co^{2+} cations.

The observed magnetism of the $Cs_2MCe_3F_{16}$ series is in stark contrast to its uranium analogs, which undergo a ferrimagnetic transition at low temperatures.[50] The magnetic structure of the uranium analogs can be described as consisting of U_3F_{22} trimers and MF_6 octahedra that form columns, which are hexagonally arranged to build up a framework. In the columns, all the uranium

atoms have the same parallel magnetic moments, while the divalent metal cations order antiferromagnetically to the uranium atoms. It was shown that the ferrimagnetic transition can be suppressed by replacing the magnetic ions Mn^{2+}, Co^{2+}, and Ni^{2+} with diamagnetic Zn^{2+} cations.[50] In a similar way, the magnetic interactions within the chains can be disrupted by replacing U^{4+} (f^2) with the diamagnetic Ce^{4+} (f^0) cations, providing further evidence for the necessity of having both divalent cations and tetravalent cations with unpaired f-electrons present for magnetic ordering to take place in $Cs_2MM'_3F_{16}$ (Figure 5).

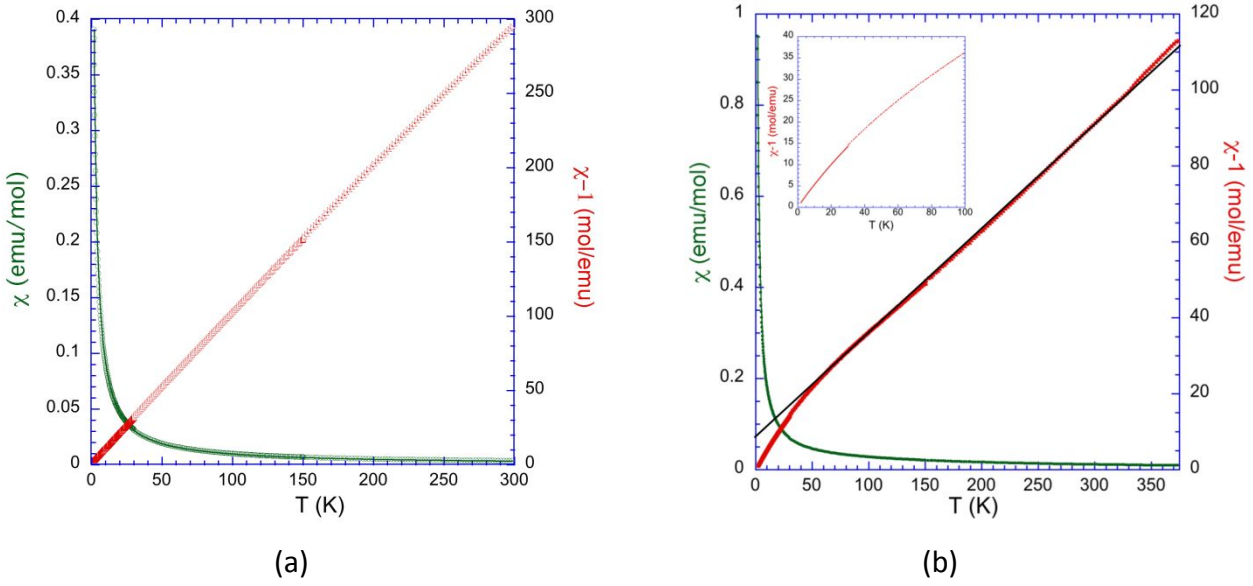

Figure 4. Magnetic susceptibility and inverse susceptibility plot of (a) $Cs_2NiCe_3F_{16}$ and (b) $Cs_2CoCe_3F_{16}$. Data were collected in a ZFC measurement with a 0.1 T applied magnetic field and are shown in the range from 2 – 300 K for $Cs_2NiCe_3F_{16}$ and 2 – 375 K for $Cs_2CoCe_3F_{16}$ phase.

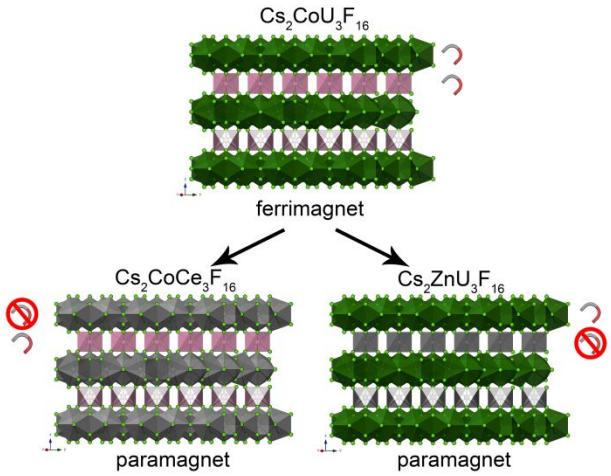

Figure 5. A schematic representation of magnetism in $Cs_2MM'_3F_{16}$ series. If both M'_3F_{16} and the M cation have unpaired electrons (paramagnetic), a magnetic ordering can be observed (e.g. $Cs_2CoU_3F_{16}$), while if either M'_3F_{16} layers or the M cation is diamagnetic, the magnetic ordering is disrupted (e.g. $Cs_2CoCe_3F_{16}$ and $Cs_2ZnU_3F_{16}$, respectively).

Table 2. Curie – Weiss Constants and Effective Magnetic Moments for the Quaternary Cerium Fluorides

Compound	θ (K)	μ_{eff}/μ_B	μ_{calc}/μ_B
$Cs_2NiCe_3F_{16}$	-4.50	2.85	2.83
$Cs_2CoCe_3F_{16}$	-26.67	5.34	3.87

Conclusion

A series of novel quaternary cerium fluorides, $Cs_2MCe_3F_{16}$ (M= Ni, Co, Mn, and Zn) $Na_3MTh_6F_{30}$ (M = Al, Ga, Fe, and Cr) was synthesized by the mild hydrothermal synthetic route and structurally characterized. The $Cs_2MCe_3F_{16}$ (M= Ni, Co, Mn, and Zn) compounds exhibit a complex three-dimensional crystal structure consisting of both corner- and edge-sharing CeF_9 polyhedra. The $Na_3MCe_6F_{30}$ structure type can structurally accommodate only smaller trivalent cations, specifically Al, Ga, Fe, and Cr in the framework. Larger trivalent cations with radii >0.645 Å do not form the target phase and simply result in the formation of CeF_3 as the major product. Magnetic susceptibility measurements for the compounds containing divalent cations Ni^{2+} and Co^{+2} ions exhibit simple paramagnetic behavior.

Acknowledgements

Financial support for this work was provided by the National Science Foundation under DMR-1806279 and is gratefully acknowledged.

Supporting Information

PXRD patterns, UV-Vis Spectra, EDS results and magnetic susceptibility versus temperature plots. CSD 1982886-1982893 contain the supplementary crystallographic data for this paper. The data can be obtained free of charge from The Cambridge Crystallographic Data Centre via www.ccdc.cam.ac.uk/structures.

References

(1) Schubert, E. F.; Kim, J. K. Solid-state light sources getting smart. *Science* **2005**, *308*, 1274-1278.
(2) Tran, T. T.; Yu, H.; Rondinelli, J. M.; Poeppelmeier, K. R.; Halasyamani, P. S. Deep Ultraviolet Nonlinear Optical Materials. *Chem. Mater.* **2016**, *28*, 5238-5258.
(3) Wang, F.; Han, Y.; Lim, C. S.; Lu, Y.; Wang, J.; Xu, J.; Chen, H.; Zhang, C.; Hong, M.; Liu, X. Simultaneous phase and size control of upconversion nanocrystals through lanthanide doping. *Nature* **2010**, *463*, 1061-1065.
(4) Zhang, F.; Braun, G. B.; Shi, Y.; Zhang, Y.; Sun, X.; Reich, N. O.; Zhao, D.; Stucky, G. Fabrication of $Ag@SiO_2@Y_2O_3$:Er Nanostructures for Bioimaging: Tuning of the Upconversion Fluorescence with Silver Nanoparticles. *J. Am. Chem. Soc.* **2010**, *132*, 2850-2851.
(5) Chen, Y.; Zhang, J. Investigation on luminescence of bifunctional $Y_{4.67}(SiO_4)_3O:Ce^{3+}/Tb^{3+}/Eu^{3+}$ phosphors. *J. Lumin.* **2020**, *218*, 116842.
(6) Choi, Y.-K.; Halappa, P.; Shivakumara, C.; Dubey, V.; Singh, V. Blue emitting Ce^{3+}-doped $CaYAl_3O_7$ phosphors prepared by combustion route. *Optik* **2019**, *181*, 1113-1121.
(7) Khan, S. A.; Jalil, A.; Ullah Khan, Q.; Irfan, R. M.; Mehmood, I.; Khan, K.; Kiani, M.; Dong, B.; Khan, N. Z.; Yu, J.-L.; Zhu, L.; Agathopoulos, S. New physical insight into crystal structure, luminescence and optical properties of $YPO_4:Dy^{3+}\backslash Eu^{3+}\backslash Tb^{3+}$ single-phase white-light-emitting phosphors. *J. Alloys Compd.* **2020**, *817*, 152687.
(8) Mayrinck, C. D.; Siqueira, R. L.; Esbenshade, J.; Schiavon, M. A.; de Lima, R. C.; Barbosa, H. P.; Lima Ribeiro, S. J.; Ferrari, J. L. Downconversion and upconversion observed from $Er^{3+}/Yb^{3+}/Eu^{3+}$ tri-doped-Y_2O_3 for application in energy conversion. *J. Alloys Compd.* **2020**, *816*, 152591.
(9) Ren, Q.-F.; Zhang, Q.-C.; Wang, S.-L.; Zheng, Q.; Ding, Y.; Jin, Z. $NaNO_3$ assistant synthesis of the olive-like $NaLa(WO_4)_2:Ln^{3+}$(Ln=Eu,Tb) structures and their luminescence properties. *Solid State Sci.* **2019**, *98*, 106026.
(10) Rubešová, K.; Havlíček, J.; Jakeš, V.; Nádherný, L.; Cajzl, J.; Pánek, D.; Parkman, T.; Beitlerova, A.; Kučerková, R.; Hájek, F.; Nikl, M. Heavily Ce^{3+}-doped $Y_3Al_5O_{12}$ thin films deposited by a polymer sol–gel method for fast scintillation detectors. *CrystEngComm* **2019**, *21*, 5115-5123.
(11) Yang, Y.; Wu, F.; Yu, H.; Hu, Y.; Qiu, C.; Li, J.; Zhang, H.; Wang, X.; Wei, L.; Liu, B. Luminescent properties of $Y_3Al_5O_{12}:Ce^{3+}$ phosphor-in-glass for WLEDs. *Optik* **2020**, *200*, 163455.
(12) Su, B.; Xie, H.; Tan, Y.; Zhao, Y.; Yang, Q.; Zhang, S. Luminescent properties, energy transfer, and thermal stability of double perovskites $La_2MgTiO_6:Sm^{3+}$, Eu^{3+}. *J. Lumin***. 2018**, *204*, 457-463.
(13)Kumar, A.; Manam, J. Color tunable emission and temperature dependent photoluminescence properties of Eu^{3+} co-doped $Gd_2Zr_2O_7:Dy^{3+}$ phosphors. *Opt. Mat.* **2019**, *96*, 109373.
(14) *Photonic and Electronic Properties of Fluoride Materials;* Tressaud, A., Poeppelmeier, K., Eds.; Elsevier: Cambridge, U.K., 2016.
(15) Du, Y.; Han, S.; Zou, Y.; Yuan, J.; Shao, C.; Jiang, X.; Chen, D. Luminescence properties of Ce^{3+}-doped oxyfluoride aluminosilicate glass and glass ceramics. *Opt. Mater.* **2019**, *89*, 243-249.

(16) Dissanayake, K. T.; Amarasinghe, D. K.; Suescun, L.; Rabuffetti, F. A. Accessing Mixed-Halide Upconverters Using Heterohaloacetate Precursors. *Chem. Mater.* **2019**, *31*, 6262-67.
(17) Dissanayake, K. T.; Rabuffetti, F. A. Multicolor Emission in Chemically and Structurally Tunable Er:Yb:SrFX (X = Cl, Br) Upconverting Nanocrystals. *Chem. Mater.* **2018**, *30*, 2453-62.
(18) Zheng, W.; Zhou, S.; Chen, Z.; Hu, P.; Liu, Y.; Tu, D.; Zhu, H.; Li, R.; Huang, M.; Chen, X. Sub-10 nm lanthanide-doped CaF_2 nanoprobes for time-resolved luminescent biodetection. *Angew. Chem.* **2013**, *52*, 6671-6676.
(19) Wang, J.; Wang, F.; Wang, C.; Liu, Z.; Liu, X. Single-band upconversion emission in lanthanide-doped $KMnF_3$ nanocrystals. *Angew. Chem.* **2011**, *50*, 10369-10372.
(20) Dhanapala, B. D.; Munasinghe, H. N.; Suescun, L.; Rabuffetti, F. A. Bimetallic Trifluoroacetates as Single-Source Precursors for Alkali-Manganese Fluoroperovskites. *Inorg. Chem.* 2017, 56, 13311-20.
(21) Wang, G.; Qin, W.; Wei, G.; Wang, L.; Zhu, P.; Kim, R.; Zhang, D.; Ding, F.; Zheng, K. Synthesis and upconversion luminescence properties of YF_3:Yb^{3+}/Tm^{3+} octahedral nanocrystals. *J. Fluorine Chem.* **2009**, *130*, 158-161.
(22) Vetrone, F.; Mahalingam, V.; Capobianco, J. A. Near-Infrared-to-Blue Upconversion in Colloidal $BaYF_5$:Tm^{3+}, Yb^{3+} Nanocrystals. *Chem. Mater.* **2009**, *21*, 1847-1851.
(23) Yongzhang Jiang, Y. J.; Haiping Xia, H. X.; Shuo Yang, S. Y.; Jiazhong Zhang, J. Z.; Dongsheng Jiang, D. J.; Cheng Wang, C. W.; Zhigang Feng, Z. F.; Jian Zhang, J. Z.; Xuemei Gu, X. G.; Jianli Zhang, J. Z.; Haochuan Jiang, H. J.; Baojiu Chen, B. C. Luminescence of Tb^{3+}/Eu^{3+} codoped $LiYF_4$ single crystals under UV excitation for white-light LEDs. *Chin. Opt. Lett.* **2015**, *13*, 071601-071605.
(24) Menyuk, N.; Pierce, J. W.; Dwight, K. NaYF4-Yb,Er - An Efficient Upconversion Phosphor. *Appl. Phys. Lett.* **1972**, *21*, 159-161.
(25) Chen, G.; Ohulchanskyy, T. Y.; Kumar, R.; Agren, H.; Prasad, P. N. Ultrasmall monodisperse $NaYF_4$:Yb(3+)/Tm(3+) nanocrystals with enhanced near-infrared to near-infrared upconversion photoluminescence. *ACS Nano* **2010**, *4*, 3163-3168.
(26)Mishra, S.; Daniele, S.; Ledoux, G.; Jeanneau, E.; Joubert, M.-F. Heterometallic Na-Y(Ln) Trifluoroacetate Diglyme Complexes as Novel Single-source Precursors for Upconverting $NaYF_4$ Nanocrystals Co-doped with Yb and Er/Tm Ions. *Chem. Commun.* **2010**, *46*, 3756− 3758.
(27)Kramer, K. W.; Biner, D.; Frei, G.; Gudel, H. U.; Hehlen, M. P.; Luthi, S. R. Hexagonal Sodium Yttrium Fluoride Based Green and Blue Emitting Upconversion Phosphors. *Chem. Mater.* **2004**, *16*, 1244−1251.
(28) Johnson, N. J. J.; Oakden, W.; Stanisz, G. J.; Scott Prosser, R.; van Veggel, F. C. J. M. Size-Tunable, Ultrasmall $NaGdF_4$ Nanoparticles: Insights into Their T1MRI Contrast Enhancement. *Chem. Mater.* **2011**, *23*, 3714-3722.
(29) Chen, Y.; Mishra, S.; Ledoux, G.; Jeanneau, E.; Daniel, M.; Zhang, J.; Daniele, S. Direct synthesis of hexagonal $NaGdF_4$ nanocrystals from a single-source precursor: upconverting $NaGdF_4$:Yb^{3+},Tm^{3+} and its composites with TiO_2 for near-IR-driven photocatalysis. *Chem. - Asian J.* **2014**, *9*, 2415-21.
(30) Barry, M. C.; Wei, Z.; He, T.; Filatov, A. S.; Dikarev, E. V. Volatile Single-Source Precursors for the Low-Temperature Preparation of Sodium-Rare Earth Metal Fluorides. *J. Am. Chem. Soc*. **2016**, *138*, 8883-87.
(31) Ju, Q.; Tu, D.; Liu, Y.; Li, R.; Zhu, H.; Chen, J.; Chen, Z.; Huang, M.; Chen, X. Amine-functionalized lanthanide-doped $KGdF_4$ nanocrystals as potential optical/magnetic multimodal bioprobes. *J. Am. Chem. Soc.* **2012**, *134*, 1323-1330.

(32) Yu, L.; Li, G.; Liu, Y.; Jiang, F.; Hong, M. Lanthanide-Doped KGd_2F_7 Nanocrystals: Controlled Synthesis, Optical Properties, and Spectroscopic Identification of the Optimum Core/Shell Architecture for Highly Enhanced Upconverting Luminescence. *Cryst. Growth Des.* **2019**, *19*, 2340-2349.
(33) Ding, Y.; Teng, X.; Zhu, H.; Wang, L.; Pei, W.; Zhu, J. J.; Huang, L.; Huang, W. Orthorhombic KSc_2F_7:Yb/Er nanorods: controlled synthesis and strong red upconversion emission. *Nanoscale* **2013**, *5*, 11928-11932.
(34) Lei, P.; An, R.; Yao, S.; Wang, Q.; Dong, L.; Xu, X.; Du, K.; Feng, J.; Zhang, H. Ultrafast Synthesis of Novel Hexagonal Phase $NaBiF_4$ Upconversion Nanoparticles at Room Temperature. *Adv. Mater.* **2017**, *29*, 1700505.
(35) Senden, T.; van Dijk-Moes, R. J. A.; Meijerink, A. Quenching of the red Mn^{4+} luminescence in Mn^{4+}-doped fluoride LED phosphors. *Light. Sci. Appl* . **2018**, *7*, 8.
(36) Ayer, G. B.; Klepov, V. V.; Smith, M. D.; zur Loye, H.-C. Mild Hydrothermal Synthesis of the Complex Hafnium-Containing Fluorides $Cs_2[M(H_2O)_6][Hf_2F_{12}]$ (M= Ni, Co, Zn), $CuHfF_6(H_2O)_4$, and $Cs_2Hf_3Mn_3F_{20}$ based on HfF_7 and HfF_6 Coordination Polyhedra. *Inorg. Chem.* **2019**, *58(19)*, 13049-13057.
(37) Underwood, C. C.; McMillen, C. D.; Kolis, J. W. Hydrothermal Synthesis and Crystal Chemistry of Novel Fluorides with $A_7B_6F_{31}$ (A = Na, K, NH4, Tl; B = Ce, Th) Compositions. *J. Chem. Crystallogr.* **2014**, *44*, 493-500.
(38) Donakowski, M. D.; Görne, A.; Vaughey, J. T.; Poeppelmeier, K. R. $AgNa(VO_2F_2)_2$: A Trioxovanadium Fluoride with Unconventional Electrochemical Properties. *J. Am. Chem. Soc*. **2013**, *135*, 9898-906.
(39) Yu, R.; Wang, D.; Takei, T.; Koizumi, H.; Kumada, N.; Kinomura, N. A Novel Open-Framework Cerium Phosphate Fluoride: $(NH_4)[CeIVF_2(PO_4)]$. *J. Solid State Chem.* **2001**, *157*, 180-185.
(40) Klepov, V. V.; Morrison, G.; zur Loye, H.-C. $Na_nMTh_6F_{30}$: A Large Family of Quaternary Thorium Fluorides. *Cryst. Growth Des.* **2019**, *19*, 1347-1355.
(41) Yeon, J.; Smith, M. D.; Morrison, G.; zur Loye, H.-C. Trivalent cation-controlled phase space of new U(IV) fluorides, $Na_3MU_6F_{30}$ (M = Al^{3+}, Ga^{3+}, Ti^{3+}, V^{3+}, $Cr^{3+,}$ Fe^{3+}): mild hydrothermal synthesis including an in situ reduction step, structures, optical, and magnetic properties. *Inorg. Chem.* **2015**, *54*, 2058-2066.
(42) Yeon, J.; Smith, M. D.; Tapp, J.; Moller, A.; zur Loye, H.-C. Application of a mild hydrothermal approach containing an in situ reduction step to the growth of single crystals of the quaternary U(IV)-containing fluorides $Na_4MU_6F_{30}$ (M = Mn^{2+}, Co^{2+}, Ni^{2+}, Cu^{2+}, and Zn^{2+}) crystal growth, structures, and magnetic properties. *J. Am. Chem. Soc* . **2014**, *136*, 3955-3963.
(43) Liu, Q.; Yin, H.; Bao, H.; Yue, Z.; Diefenbach, K.; Tang, Z.; Lin, J.; Wang, J.-Q. Insights into the new 3d–5f heterometallic quaternary fluorides: Synthesis, crystal structures, spectroscopic properties, and thermodynamic stability. *Inorganica Chimica Acta* **2019**, *487*, 362-368.
(44) Shannon, R. D. Revised effective ionic radii and systematic studies of interatomic distances in halides and chalcogenides. *Acta Crystallogr., Sect. A: Cryst. Phys., Diffr., Theor. Gen. Crystallogr.* **1976**, *32*, 751-767.
(45) *SAINT*; Bruker AXS Inc.: Madison, WI, USA, 2012.
(46) Krause, L.; Herbst-Irmer, R.; Sheldrick, G. M.; Stalke, D. Comparison of silver and molybdenum microfocus X-ray sources for single-crystal structure determination. *J. Appl. Crystallogr.* **2015**, *48*, 3-10.

(47) Sheldrick, G. M. Crystal structure refinement with SHELXL. *Acta Crystallogr., Sect. C: Struct. Chem.* **2015**, *71*, 3-8.
(48) Kubelka, P.; Munk, F. A contribution to the look of the paints. *Z. Technol. Phys.* **1931**, *12*, 593.
(49) Morrison, G.; zur Loye, H.-C. Simple correction for the sample shape and radial offset effects on SQUID magnetometers: Magnetic measurements on Ln_2O_3 (Ln=Gd, Dy, Er) standards. *J. Solid State Chem.* **2015**, *221*, 334-337.
(50) Klepov, V. V.; Pace, K. A.; Calder, S.; Felder, J. B.; zur Loye, H.-C. 3d-Metal Induced Magnetic Ordering on U(IV) Atoms as a Route toward U(IV) Magnetic Materials. *J. Am. Chem. Soc.* **2019**, *141*, 3838-3842.
(51) Tanabe, Y.; Sugano, S. On the Absorption Spectra of Complex Ions, III The Calculation of the Crystalline Field Strength. *J. Phys. Soc. Jpn.* **1956**, *11*, 864-77.

Table of Content

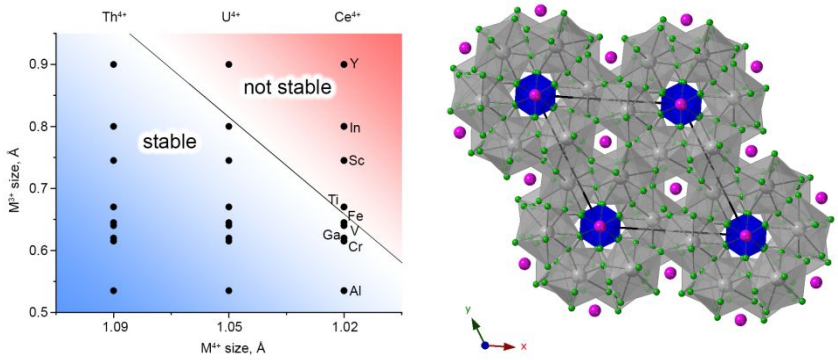

A view of the size of trivalent cations M^{3+} (M = Al, Cr, Ga, V, Fe, Ti, Sc, In, and Y) plotted against the size of the tetravalent framework forming cations Th^{4+}, U^{4+}, and Ce^{4+} and a complex 3D framework structure of $Na_3MCe_6F_{30}$ (M = Al, Ga, Fe, and Cr) along the c-axes.